Energy & Environmental Science

Dynamic Article Links ▶

COMMUNICATION

Hierarchical TiO$_2$–Si nanowire architecture with photoelectrochemical activity under visible light illumination†

Jian Shi and Xudong Wang*

Bandgap engineering of TiO$_2$ is a substantial strategy for efficient water splitting in the visible light range. Introducing dopants and hydrogenation have been found effective for that purpose. In this paper, we report the development of a hierarchical three dimensional TiO$_2$–Si nanowire (NW)-based photoelectrochemical (PEC) anode with visible light photochemical activity. The TiO$_2$ NWs were synthesized using a surface reaction-limited pulsed chemical vapor deposition method (SPCVD) with unbalanced TiCl$_4$ and H$_2$O precursors. Dangling Ti–Cl and Ti–OH groups inside TiO$_2$ NW crystals were suggested to be the reason for band narrowing and visible light absorption. The NW structure with a large aspect ratio was formed *via* the oriented attachment mechanism, which offered a super-high surface area density. This *in situ* crystal decoration approach opens a new window to tailoring electrical properties of TiO$_2$ for wider spectrum solar energy harvesting and conversion.

Owing to the abundance, cleanness, potentially low-cost, and the environmentally benign nature of solar energy, production of hydrogen fuel from photocatalyzed water splitting (or water photolysis) is of fundamental importance to alleviate or solve the problem that fossil resources confront.[1–4] Nevertheless, the efficiencies of most semiconductor-based solar-to-chemical energy conversion

Department of Materials Science and Engineering, University of Wisconsin-Madison, Madison, WI 53706, USA. E-mail: xudong@engr. wisc.edu
† Electronic supplementary information (ESI) available. See DOI: 10.1039/c2ee22113f

systems are currently less competitive than common solar panels, which to a great extent limits the commercialization of photolysis technology.[5–7] To achieve desired water photolysis efficiency, endeavors have been carried out from various aspects. For example, to engineer the semiconductor valence and conduction bands so that they properly straddle the water redox potentials is substantial for maximizing theoretical photochemical efficiency.[8] Another criterion for low-cost photolysis is the long-term stability of the semiconductor in water or electrolytes. Various engineering methods had been implemented to make resilient semiconducting photocatalysts.[9] Other critical issues include light absorption and charge transfer dynamics inside the materials and through the semiconductor–electrolyte interfaces.[10–14]

Titanium dioxide (TiO$_2$) is a promising photoactive material that has been extensively studied for catalyzing photoelectrochemical (PEC) water splitting.[8,15] It offers several compelling advantages including low cost, high chemical stability, excellent photocorrosion resistance, and superior quantum efficiency in the UV range.[5] Recently, we developed a surface reaction-limited pulsed chemical vapor deposition (SPCVD) technique that realized a novel high-density 3D TiO$_2$ branch–Si nanowire (NW) architecture.[14,16,17] The 3D NW architecture offered super high surface area density as well as excellent charge transport properties, and thus it yielded a nearly three-times higher PEC efficiency compared to straight NW structures with only UV light absorption.

Although TiO$_2$ is very promising in the UV range, the potential energy manifested by the deviation between the valence band of TiO$_2$ and the water oxidation potential does not participate in the photochemical process, which dramatically reduces the PEC efficiency.

Broader context

Realization of water splitting by TiO$_2$ under visible light illumination is an inevitable step towards commercialization of TiO$_2$ photochemical application. We report a new strategy to enable visible light absorption of TiO$_2$ nanowires by modifying our previously developed surface reaction-limited pulsed CVD technique (SPCVD), in which the water dose was extended and TiCl$_4$ precursor was supplied with a limited amount during each cycle. It was suggested that the large amount of residual Ti–OH and Ti–Cl may contribute to the visible light activity of TiO$_2$ nanowires. X-ray photoelectron spectroscopy reveals that the valence band of SPCVD TiO$_2$ nanowire is raised up by about 2.0 eV compared to un-doped ones. The TiO$_2$ nanowires were grown as branches uniformly covering dense and high aspect ratio Si nanowire templates. Such a three dimensional nanowire network has a very large surface area and demonstrated high efficiency under simulated illumination and considerable photoactivity in the visible light region. The SPCVD method enriches the doping knowledge and sheds light on developing high efficiency photoelectrodes.

Meanwhile, the wide bandgap of TiO_2 (3.4 eV) rules out the absorption and utilization of visible light that holds a dominant percentage in the AM 1.5G solar spectrum. These two intrinsic limitations have to be addressed for achieving high PEC efficiency. Doping of TiO_2 with foreign elements has been investigated to introduce localized states above valence band maximum, enabling PEC activity in the visible light range.[18–24] Hydrogenation has also been found as an effective method to narrow the bandgap of TiO_2 by creating mid-gap states, which is believed to be the result of disordered structure with dangling Ti–OH and Ti–H groups.[25] Such "black TiO_2" exhibited highly efficient photochemical water splitting in the visible light range. In this paper, we report a development of –OH and –Cl decorated anatase TiO_2 NWs grown on dense Si NW backbones *via* the SPCVD method. Visible light photochemical activity was demonstrated by using these TiO_2–Si 3D NW architectures as the PEC anode. This result evidenced the ability of the SPCVD technique in creating composition- and property-controlled 3D NW architectures and extended the excellent photochemical activity of our previously developed TiO_2–Si NW heterostructures from UV to visible light range.

In the TiO_2–Si 3D NW architecture, Si NWs act as conductive paths for fast electron transportation, while water oxidation occurs on the TiO_2 NW surfaces. The Si NW arrays were made by wet-chemical etching a highly doped Si substrate.[12] Cross-sectional and planar views of the as-etched Si NWs are shown in Fig. S1†. The length of Si NWs was ∼20 μm for the growth of TiO_2 NW branches by the SPCVD technique, where increased water exposures and reduced $TiCl_4$ exposures were applied. A detailed growth setup can be found in the ESI†. The as-synthesized sample appeared pure black indicating effective absorption of visible light (inset of Fig. 1a). The UV-Vis absorption spectrum demonstrates that the absorption edge of the as-synthesized TiO_2 NWs on the fluorine-doped tin oxide (FTO) substrate locates at 600 nm (Fig. S2†). A scanning electron microscopy (SEM) image of the sample surface confirmed the universal coating of TiO_2 NWs everywhere across the Si NW substrate (Fig. 1a). The cone-shaped pillars were a result of the capillary-force-induced Si NW bundling during the chemical etching process. A closer view showed high density TiO_2 NWs anchoring on the Si NW bundles (Fig. 1b). These TiO_2 NWs exhibited a larger aspect ratio than those made *via* the regular SPCVD process. They were typically 20–30 nm in diameter and ∼500 to 600 nm long with a very narrow dimensional distribution. Fig. 1c shows a cross-sectional view of a 20 μm-long Si NW template coated with high-density TiO_2 NWs, where the Si NW bundles can also be observed. The fuzzy surfaces indicated a complete coverage of TiO_2 NWs over the entire Si NW arrays. High magnification SEM images acquired from dashed box region shown in Fig. 1c clearly revealed the uniform and high-density coating of TiO_2 NWs on the buddle tip (Fig. 1d) as well as deep inside the inter-bundle spaces (Fig. 1e) with great integrity. The TiO_2 NWs in these inter-bundle spaces exhibited similar dimensions and morphologies as those observed on the top rims. Closer observation revealed that all the TiO_2 NWs had a necklace-like structure that was composed of coherent nanocrystals with nearly identical sizes and diamond-like shapes.

The phase of the as-synthesized TiO_2 NWs was identified to be anatase by X-ray diffraction (XRD) (Fig. S3†). To further understand the structure and crystallography of the TiO_2 NWs, a series of characterizations by transmission electron microscopy (TEM) and selective-area electron diffraction (SAED) were conducted. Fig. 2a is
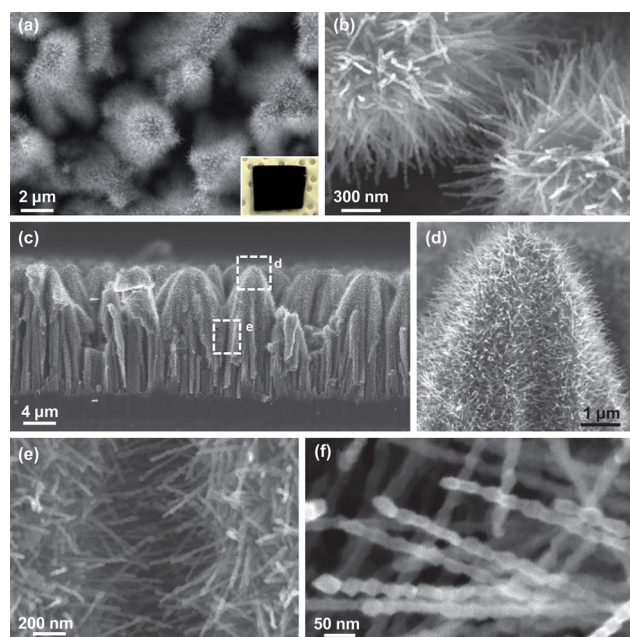

Fig. 1 Morphology of TiO_2–Si NW 3D architecture. (a) Planar view of the surface of TiO_2 NW-coated high-density Si NW arrays. Inset is a photo of an as-synthesized sample. (b) Closer view of TiO_2 NW morphology showing the rough surface and typical dimensions. (c) Cross-section of the TiO_2–Si NW architectures, where the Si NW templates were ∼20 μm long. (d) High magnification SEM image of the top rim of a Si NW bundle covered with dense TiO_2 NWs pointing outward. (e) Highly packed TiO_2 NWs filled the narrow space between adjacent Si NWs. (f) Necklace structure of TiO_2 NW composed of coherent nanocrystals.

a bright field TEM image of dispersed TiO_2 NWs, where a narrow diameter distribution (26 nm ± 5 nm) can be observed. The non-uniform contrast on some NWs indicates that there may exist lattice twisting within single NWs. It was also observed that the nanocrystals composed of the NWs were not identical and exhibited slightly variable sizes and shapes (Fig. 2b). SAED characterizations from different locations along the NW demonstrated that the entire NW was a single crystal with the growth direction along the [002] (inset of Fig. 2b). The anatase phase of the NW could also be confirmed by the diffraction pattern. High resolution TEM (HRTEM) revealed the high quality lattice of the NWs without the presence of line or facet defects in each nanocrystal period (Fig. 2c). The lattice spacings acquired from the HRTEM image matched the reported ones well, with (002) being 0.48 nm and (011) 0.35 nm.

HRTEM also indicated the existence of overlapped lattice structures in the contact region between two adjacent nanocrystals (Fig. 2d), which signified that the growth mechanism of the TiO_2 NWs was likely to be the oriented attachment mode.[26–29] Similar TiO_2 NW structures prepared either in solution or by vapor deposition have been reported.[30] In the orientation attachment mechanism, as-formed nanocrystals tend to configure each other by joining together through the highest surface energy facet, anatase TiO_2 (002) in our case, and fashion into necklace-like NW morphology. The possible misalignment between neighboring nanocrystals could give birth to a non-uniform contrast within a single NW. During this SPCVD growth process, the exposure of water precursor was twice as much as that used in a regular SPCVD which produced straight TiO_2
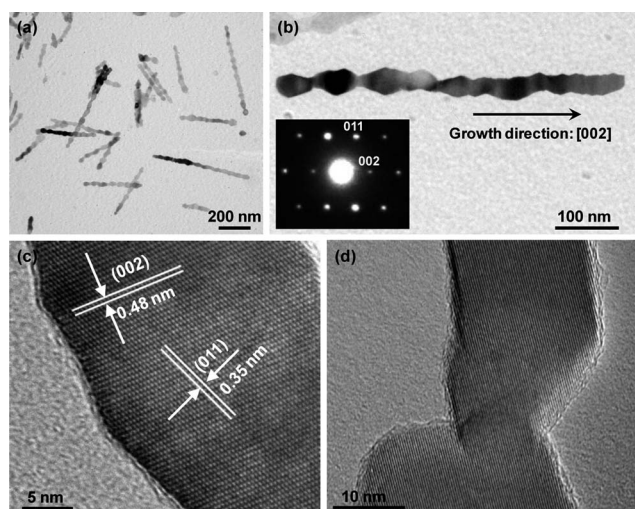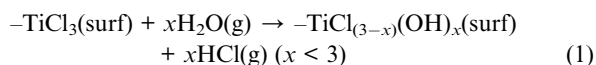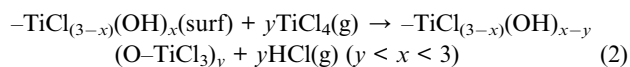
Fig. 2 TEM analysis of TiO₂ NWs. (a) TEM image of TiO₂ NWs showing their uniform thickness. (b) Image of a single NW showing the possible twisting structure of NW formed by the oriented attachment mechanism. The NW was a single crystal and grew along the [002] direction. Inset is the SAED pattern of the NW confirming the anatase phase and growth orientation. (c) HRTEM image of a TiO₂ NW showing perfect and dislocation-free lattice structure. The measured lattice spacings matched well with standard data. (d) HRTEM image of an overlapped region acquired from the boundary of two neighboring nanocrystals revealing the oriented attachment mode.

NWs. Since water molecules could be absorbed onto the particle surfaces improving the mobility of TiO₂ nanocrystals for spontaneous self-organization, the deposition environment with an extra amount of water in the growth chamber was therefore favorable for the oriented attachment mechanism.

In order to understand the visible light absorption capability of the TiO₂ NWs, X-ray photoelectron spectroscopy (XPS) was applied to analyze the bonding states of Ti and O. Fig. 3a shows the XPS spectrum of as-synthesized TiO₂ NWs grown on Si NW backbones, from which the characteristic peaks of Ti, C, O, and Si can be clearly observed. The Ti 2p, Ti 3s, and Ti 3p peaks are identical to commercial P25 TiO₂ particles. A small signal from Cl was also detected (top inset of Fig. 3a), evidencing the existence of residue Cl. Cl is a common impurity in most $TiCl_4/H_2O$ atomic layer deposition (ALD) products and is believed to be a result of the incomplete reaction of surface –Cl functional groups, as shown in eqn (1):

$$-TiCl_3(surf) + xH_2O(g) \rightarrow -TiCl_{(3-x)}(OH)_x(surf) + xHCl(g)\ (x < 3) \quad (1)$$

A strong peak corresponding to O 1s with the bonding state as Ti–O–H also appeared at 532.5 eV. Similar to the residue Cl, the presence of Ti–O–H bonds is believed to be due to the incomplete reaction of surface –OH groups, as shown in eqn (2):

$$-TiCl_{(3-x)}(OH)_x(surf) + yTiCl_4(g) \rightarrow -TiCl_{(3-x)}(OH)_{x-y}(O-TiCl_3)_y + yHCl(g)\ (y < x < 3) \quad (2)$$

The incompletion of –OH reaction could be further exaggerated when supply of TiCl₄ was limited and/or physically adsorbed water molecules were not completely desorbed from the crystal surfaces.
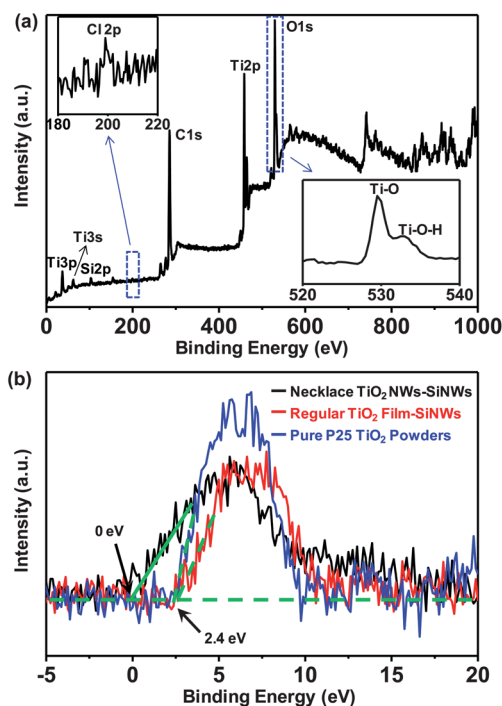

Fig. 3 XPS analysis of bonding state of TiO₂ NWs. (a) Full range XPS spectrum obtained from as-synthesized TiO₂–Si NW heterostructure. The characteristic peaks are identified to be the same as commercial P25 TiO₂ particles except that Cl 2p (left inset) and O1s from Ti–O–H bonds (right inset) were found to be unique for this structure. (b) Valence band XPS demonstrates that new states appeared in the vicinity of valence band maximum for NW morphology which could provide photochemical activity in the visible light region.

Therefore, in our modified SPCVD growth, an appreciable amount of –OH groups was left inside the TiO₂ NW lattices. The HRTEM images shown in Fig. 2 revealed that there was no disordered or amorphous structure in the NW. We therefore believe that the dangling Ti–OH and Ti–Cl groups only sparsely distributed along the broken shared edges of TiO₂ octahedrons in the anatase phase. Their concentration may not be high enough to destroy the lattice and create an amorphous phase. This situation is different from the hydrogenation case, where H₂ breaks Ti–O–Ti bonds into Ti–OH and Ti–H, and turns the crystalline structure near surface into amorphous.[25] Nevertheless, in our case, similar dangling groups Ti–OH and Ti–Cl existed in the lattice and this may make likewise contributions toward the band structure, *i.e.* creating mid-band states in TiO₂. The density of states (DOS) of the valence band of the TiO₂ NWs was therefore obtained by XPS and compared to regular TiO₂ structures. Valence band maximum of the TiO₂ NWs was lifted up to 0 eV from 2.4 eV of regular TiO₂ nanorods synthesized by the SPCVD method and as-purchased P25 TiO₂ powders (Fig. 3b). The increase of valence band maximum indicates narrowing of the bandgap and makes it possible for the TiO₂ NWs to absorb photons in the visible light range. The modified band configuration could positively augment the PEC efficiency due to visible light absorption and properly straddled band alignment between the TiO₂ NWs and the water redox potentials.

To investigate the photochemical activity of the bandgap-modified TiO₂ NWs, PEC cells were fabricated and characterized under

7920 | *Energy Environ. Sci.*, 2012, **5**, 7918–7922

This journal is © The Royal Society of Chemistry 2012

different wavelengths of illumination. Before measurement, the TiO_2–Si NW heterostructure was coated with a thin film of poly-crystalline anatase TiO_2 to isolate the Si surface from the electrolyte. Detailed procedures for fabricating PEC cells and measurement setup can be found in the ESI†. Photochemical activity of the TiO_2–Si NW architecture with 25 nm TiO_2 overcoating is presented in Fig. 4a. Under 100 mW cm^{-2} illumination of a full spectrum solar simulator, the short circuit photocurrent density approached 2.7 mA cm^{-2}, which was fairly competitive compared to other reported TiO_2 PEC anodes.[1,14] The decent fill factor of the PEC cell evidenced an excellent charge separation rate, indicating high quality material interfaces and crystallinity of the TiO_2 NWs. The extremely low dark current density of the anode suggested that the minority defects of NW architecture were very low.

The photochemical activity under visible light was further investigated by applying either a UV filter or green light filter to the solar simulator. Onset wavelength of the UV filter was located at 400 nm, which is also the absorption edge of regular un-doped TiO_2. The

green light filter only allowed light with a wavelength ranging from 500 nm to 600 nm to pass (Fig. S4†). J–E curves of the same TiO_2–Si NW PEC anode measured under full visible light illumination (UV filter applied) and green light illumination (green light filter applied) are shown in Fig. 4b. When the applied potential was 0.5 V versus SCE, the photocurrent densities reached 0.8 mA cm^{-2} and 0.4 mA cm^{-2}, respectively. The appreciable photocurrent suggests that a considerable amount of water oxidation reactions was catalyzed by incident photons in the visible wavelength range. The drastic decrease of the fill factor and the PEC efficiency was likely a consequence of the introduction of interband states, which facilitated the recombination of photoexcited electrons and holes while making contribution to the photolysis process. To rule out the possible photocurrent contribution from Si NW, J–E measurement was conducted on the Si NWs with an ALD-type 25 nm thick TiO_2 film under green light illumination, as shown in Fig. S5†. It demonstrates that there is no sensible photocurrent from Si NWs.

In addition, the protective TiO_2 overcoating was another important factor that influenced photochemical activity of TiO_2 NWs under visible light. It is a fact that the ALD TiO_2 film does not contribute any photocurrent in the visible light range, but it could scatter or redirect the visible light and reduce the light intensity that reaches the TiO_2 NWs. The overcoating effect was demonstrated by potentiostatic measurements on the TiO_2–Si NW PEC anode with different thickness TiO_2 overcoatings, in which the applied potential was fixed at 0 V vs. SCE (Fig. 4c). When illuminated under green light, the photocurrent densities were detected to be 0.10, 0.07, and 0.015 mA cm^{-2} corresponding to 0, 10, and 25 nm overcoating thickness, respectively. This observation also confirmed that the active component for photolysis under visible light was the TiO_2 NWs. The inset of Fig. 4c illustrates the relations between overcoating thicknesses and photocurrent densities, which could be utilized as guidance for PEC anode optimization to balance the long-term stability and the PEC efficiency.

TiO_2 NWs with a narrowed bandgap were grown on high density Si NW arrays via the SPCVD approach. The as-received TiO_2 NWs exhibited uniform and dense coverage over the entire Si NW surfaces. Regulating the exposure of H_2O and $TiCl_4$ precursors generated an appreciable amount of Ti–OH and Ti–Cl species in the TiO_2 NW lattice, which are believed to be responsible for the increase of valance band maximum. PEC measurements demonstrated that the TiO_2–Si NW anodes were fairly competitive in photocatalyzed water splitting under simulated solar illumination. Appreciable photochemical activity was also observed in the visible light range due to the narrowed bandgap. Nevertheless, the interband states may also facilitate electron–hole recombination and lower the PEC efficiency. This research demonstrated the powerfulness of the SPCVD technique in controlling the composition and physical properties of branched 3D NW architectures. In addition to enlarging the surface area density, a new pathway was created by the SPCVD technique to engineer the electrical properties of nanomaterials for efficient solar energy harvesting and conversion.
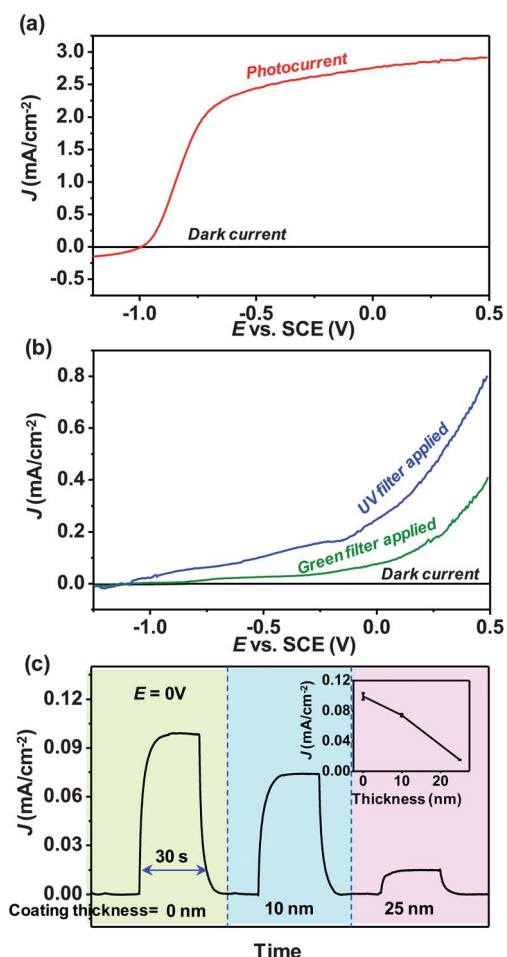

Fig. 4 PEC characterizations of TiO_2–Si 3D NW anode. (a) J–E plot of typical TiO_2–Si NW 3D PEC electrode with 25 nm overcoating. The sample was illuminated by a solar simulator with a light intensity of 100 mW cm^{-2}. (b) J–E plots of the same PEC anode when UV filter and green light filter were applied. Appreciable photocurrents were detected under visible light illumination. (c) Potentiostat measurements of NW anodes without coating (0 nm), with coating of 10 nm and 25 nm. Inset is the plot of the maximum photocurrent density versus coating thickness.

Acknowledgements

References

1 X. B. Chen, S. H. Shen, L. J. Guo and S. S. Mao, *Chem. Rev.*, 2010, **110**, 6503–6570.
2 A. Currao, *Chimia*, 2007, **61**, 815–819.
3 A. Fujishima and K. Honda, *Nature*, 1972, **238**, 37–38.
4 M. Gratzel, *Nature*, 2001, **414**, 338–344.
5 T. Bak, J. Nowotny, M. Rekas and C. C. Sorrell, *Int. J. Hydrogen Energy*, 2002, **27**, 991–1022.
6 K. Maeda and K. Domen, *J. Phys. Chem. Lett.*, 2010, **1**, 2655–2661.
7 M. G. Walter, E. L. Warren, J. R. McKone, S. W. Boettcher, Q. X. Mi, E. A. Santori and N. S. Lewis, *Chem. Rev.*, 2010, **110**, 6446–6473.
8 O. Carp, C. L. Huisman and A. Reller, *Prog. Solid State Chem.*, 2004, **32**, 33–177.
9 S. Takabayashi, R. Nakamura and Y. Nakato, *J. Photochem. Photobiol., A*, 2004, **166**, 107–113.
10 S. W. Boettcher, J. M. Spurgeon, M. C. Putnam, E. L. Warren, D. B. Turner-Evans, M. D. Kelzenberg, J. R. Maiolo, H. A. Atwater and N. S. Lewis, *Science*, 2010, **327**, 185–187.
11 S. W. Boettcher, E. L. Warren, M. C. Putnam, E. A. Santori, D. Turner-Evans, M. D. Kelzenberg, M. G. Walter, J. R. McKone, B. S. Brunschwig, H. A. Atwater and N. S. Lewis, *J. Am. Chem. Soc.*, 2011, **133**, 1216–1219.
12 Y. J. Hwang, A. Boukai and P. D. Yang, *Nano Lett.*, 2009, **9**, 410–415.
13 Z. W. Liu, W. B. Hou, P. Pavaskar, M. Aykol and S. B. Cronin, *Nano Lett.*, 2011, **11**, 1111–1116.
14 J. Shi, Y. Hara, C. L. Sun, M. A. Anderson and X. D. Wang, *Nano Lett.*, 2011, **11**, 3413–3419.
15 K. Shankar, J. I. Basham, N. K. Allam, O. K. Varghese, G. K. Mor, X. J. Feng, M. Paulose, J. A. Seabold, K. S. Choi and C. A. Grimes, *J. Phys. Chem. C*, 2009, **113**, 6327–6359.
16 J. Shi, C. L. Sun, M. B. Starr and X. D. Wang, *Nano Lett.*, 2011, **11**, 624–631.
17 J. Shi and X. D. Wang, *Cryst. Growth Des.*, 2011, **11**, 949–954.
18 J. H. Kim, T. K. Yun, J. Y. Bae and K. S. Ahn, *Jpn. J. Appl. Phys.*, 2009, **48**, 120204-1–120204-3.
19 H. Morisaki, M. Hariya and K. Yazawa, *Appl. Phys. Lett.*, 1977, **30**, 7–9.
20 J. H. Park, S. Kim and A. J. Bard, *Nano Lett.*, 2006, **6**, 24–28.
21 K. R. Reyes-Gil, E. A. Reyes-Garcia and D. Raftery, *J. Electrochem. Soc.*, 2006, **153**, A1296–A1301.
22 S. Sakthivel, M. Janczarek and H. Kisch, *J. Phys. Chem. B*, 2004, **108**, 19384–19387.
23 J. J. Sene, W. A. Zeltner and M. A. Anderson, *J. Phys. Chem. B*, 2003, **107**, 1597–1603.
24 J. Wang, D. N. Tafen, J. P. Lewis, Z. L. Hong, A. Manivannan, M. J. Zhi, M. Li and N. Q. Wu, *J. Am. Chem. Soc.*, 2009, **131**, 12290–12297.
25 X. B. Chen, L. Liu, P. Y. Yu and S. S. Mao, *Science*, 2011, **331**, 746–750.
26 N. D. Burrows, V. M. Yuwono and R. L. Penn, *MRS Bull.*, 2011, **35**, 133–137.
27 R. L. Penn, *J. Phys. Chem. B*, 2004, **108**, 12707–12712.
28 R. L. Penn and J. F. Banfield, *Science*, 1998, **281**, 969–971.
29 R. L. Penn, K. Tanaka and J. Erbs, *J. Cryst. Growth*, 2007, **309**, 97–102.
30 Y. Guyodo, A. Mostrom, R. L. Penn and S. K. Banerjee, *Geophys. Res. Lett.*, 2003, **30**, DOI: 10.1029/2003GL017021.